ARL-TR-8471 ● AUG 2018

US Army Research Laboratory

Low-Cost Actuator Dynamic Model and Controller Development for Gun-Launched Munitions

by Joshua T Bryson and Frank E Fresconi

NOTICES

Disclaimers

The findings in this report are not to be construed as an official Department of the Army position unless so designated by other authorized documents.

Citation of manufacturer's or trade names does not constitute an official endorsement or approval of the use thereof.

Destroy this report when it is no longer needed. Do not return it to the originator.

ARL-TR-8471 ● AUG 2018

US Army Research Laboratory

Low-Cost Actuator Dynamic Model and Controller Development for Gun-Launched Munitions

by Joshua T Bryson and Frank E Fresconi
Weapons and Materials Research Directorate, ARL

REPORT DOCUMENTATION PAGE

Form Approved
OMB No. 0704-0188

1. REPORT DATE *(DD-MM-YYYY)*	2. REPORT TYPE	3. DATES COVERED (- To)
August 2018	Technical Report	December 2017–March 2018

4. TITLE AND SUBTITLE
Low-Cost Actuator Dynamic Model and Controller Development for Gun-Launched Munitions

5a. CONTRACT NUMBER

5b. GRANT NUMBER

5c. PROGRAM ELEMENT NUMBER

6. AUTHOR(S)
Joshua T Bryson and Frank E Fresconi

5d. PROJECT NUMBER

5e. TASK NUMBER

5f. WORK UNIT NUMBER

7. PERFORMING ORGANIZATION NAME(S) AND ADDRESS(ES)
US Army Research Laboratory
ATTN: RDRL-WML-E
Aberdeen Proving Ground, MD 21005

8. PERFORMING ORGANIZATION REPORT NUMBER
ARL-TR-8471

9. SPONSORING/MONITORING AGENCY NAME(S) AND ADDRESS(ES)

10. SPONSOR/MONITOR'S ACRONYM(S)

11. SPONSOR/MONITOR'S REPORT NUMBER(S)

12. DISTRIBUTION/AVAILABILITY STATEMENT
Approved for public release; distribution is unlimited.

13. SUPPLEMENTARY NOTES

14. ABSTRACT
The US Army's modernization priority of long-range precision fires has highlighted a need for low-cost, high-g survivable, fast-responding munition control actuation technologies to enable range extension and terminal maneuvers. This report focuses on research into independent canard control actuator technologies based on commercial off-the-shelf servomotors. Linear and nonlinear actuator dynamic models are presented, and the model parameters are estimated from open-loop experiment results. An optimal, model-based controller is developed for the actuator. This controller was implemented in hardware, and an experiment was performed to demonstrate the closed-loop response of the actuator satisfies the design requirements.

15. SUBJECT TERMS
actuator dynamics and control, system identification, linear quadratic integrator, model-based control, canard control actuation system

16. SECURITY CLASSIFICATION OF:			17. LIMITATION OF ABSTRACT	18. NUMBER OF PAGES	19a. NAME OF RESPONSIBLE PERSON
a. REPORT	b. ABSTRACT	c. THIS PAGE			Joshua T Bryson
Unclassified	Unclassified	Unclassified	UU	28	19b. TELEPHONE NUMBER (Include area code) 410-306-1939

Contents

List of Figures

List of Tables

Acknowledgments

The authors are grateful to Mark Ilg and Jim Maley for assistance with the electronics, embedded processing, and controller development.

1. Introduction

The Army's modernization priority of long-range precision fires is motivating research into maneuvering projectile technologies for gun-launched munitions in order to provide terminal maneuver authority to engage targets with precision, as well as range extension by shaping the trajectory. Enhancing munition maneuverability is a multidisciplinary effort influenced by a variety of factors including airframe dynamics, aerodynamics, and the control actuation system. This research is focused on understanding the actuator dynamics to develop canard control technologies.

A significant challenge to developing actuation technologies for the gun-launched environment is the high-g loads experienced by the electromechanical components during the gun-launch event.[1] Along with the launch survivability challenges, the flight velocities and dynamics typically result in actuator requirements that demand a fast, precise response.

Cost is also a significant constraint for actuator development. The control actuation system is typically a significant driver of guided munition cost, and more expensive munitions are purchased in smaller quantities and tend to be employed more sparingly. Prioritizing low-cost control actuation technologies helps preserve the high-volume fire capabilities and deep magazines typical of gun-based weapon systems, while improving the range and terminal control authority maneuverability of the munition and providing range.

Currently fielded gun-launched guided munitions make use of repurposed tactical missile or aerospace actuator technologies and harden them for the high-g gun launch.[2,3] These high-performance actuators provide desired maneuverability but significantly add to the overall munition cost. Recent research has successfully demonstrated an under-actuated solution that uses fewer actuators to reduce cost by dithering a canard in phase with the projectile roll.[4–7] However, this inherent modulation of the control surface means this approach is better suited to small course corrections and is not well suited to high-maneuverability applications. Other research into maneuverability technologies has pursued the concept of generating asymmetric aerodynamic forces on the projectile body by injecting pulsed jets[8] or plasma into the flow,[9] or by modulating protrusions to create desirable shock interactions on fixed fins.[10,11] These approaches are survivable to high-g loads, but offer limited maneuverability and are only effective across limited flight regimes. Another approach uses piezoelectric actuators to morph an airfoil.[12] This concept is also well suited to high-g launch survivability but offers only

limited maneuverability due to the power requirements of piezoelectric actuation over large deflections.

The overarching goal of this research is to realize low-cost, fast-responding, high-g tolerant control actuation technologies for guided munitions. Low-cost, commercial off-the-self (COTS) technologies are adapted into a high-g survivable, independent canard control actuator that meets flight performance requirements. This report describes the development of linear and nonlinear actuator dynamic models that are used to design an optimal controller that meets the actuator performance objectives and can be used in system-level modeling to improve fidelity of actuator performance requirements.

This report is organized as follows: the technology demonstration airframe and actuator are outlined in Section 2, the linear and nonlinear actuator dynamic models are presented in Section 3, and the controller architecture is described in Section 4. An overview of the dynamic model parameter identification algorithm is presented in Section 5. An experiment is presented to measure the open-loop actuator response in Sections 6 and 7, and the results are used to estimate the parameters of the actuator dynamic models in Section 8. Finally, in Sections 9 and 10, a controller is implemented and the performance of the closed-loop system response is demonstrated to meet objectives both in simulation and experiment.

2. Airframe and Control Actuation

Figure 1 illustrates a high-maneuverability airframe (HMA) used for technology demonstration purposes. The munition is 83 mm in diameter, 420 mm long, weighs about 3.3 kg, and flies in the subsonic regime after experiencing up to 10,000 g's of acceleration during gun launch. The vehicle features eight fixed fins in the rear for stabilization and four moveable canards toward the nose for control.[13]

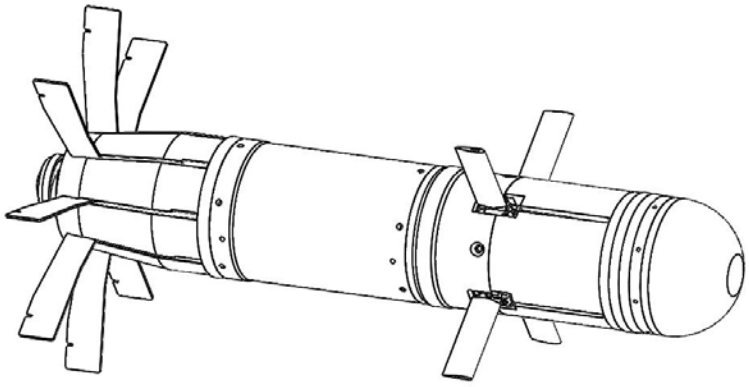

Fig. 1 Illustration of the 83-mm, gun-launched, HMA showing the four independently controlled canards near the projectile nose

Canards are independently deflected with a ±10° range through a control actuation system (CAS). The canards are actuated through a rigid bar linkage using an E-flite EFLRDS76T servomotor (hereafter referred to as servo) that has been modified by removing the stock electronic control circuitry. A digital signal processor (DSP) runs a custom controller to actuate all four canards to deflection angles provided by a flight control algorithm using the stock servos, gear train, and output shaft potentiometer.[14] Figure 2 shows the EFLRDS76T stock servo, and Fig. 3 shows the servo integrated into the assembly, actuating the canard through the linkage.

Fig. 2 The E-flite EFLRDS76T off-the-shelf servo used in the CAS

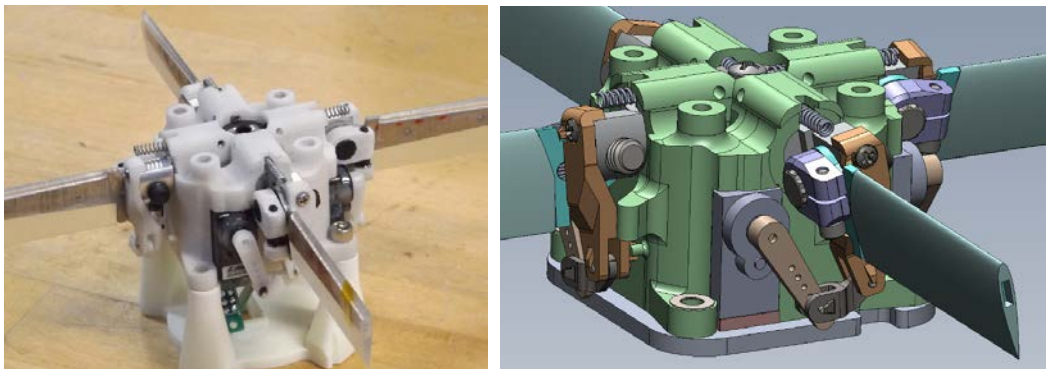

Fig. 3 The CAS showing the servo actuating the canard blade

A goal for this research is to keep the cost of each projectile low; COTS components are preferred where possible. The CAS is designed to use COTS hobby-grade servos to actuate the canards; however, the stock controller packaged with the servo is not sufficient to provide the performance required for this application. Developing a custom controller with faster response times enables the CAS to make use of the low-cost COTS servo hardware, while still offering the performance required to control a gun-launched projectile.

To improve the servo performance in the current CAS design, this research seeks to implement a custom motor controller to drive the servos. The stock electronics

are removed from the servo housing, leaving only the brushed DC motor, the nylon gear-train, and the output shaft potentiometer. A DSP interfaces with the potentiometers of all four servos and runs a custom controller to control the canard position by changing the voltage applied to the servo motors.

3. Actuator Dynamic Models

A dynamic model that accurately characterizes the actuator transient behavior is critical to the development of a fast, accurate controller. This research seeks to identify 1) a linear, lumped parameter dynamic model for the servo, linkage, and canard blade to use in controller formulation and 2) a physics-based, nonlinear dynamic model to use in controller simulation and performance evaluation, and to represent the actuator behavior in flight simulations.

3.1 Linear Dynamic Model

A linear, lumped parameter dynamic model describing the behavior of the actuator is given by the following:

$$\ddot{\delta} + 2\zeta\omega_n\dot{\delta} + \omega_n^2\delta = \omega_n^2 K V_{CMD}, \tag{1}$$

with δ, $\dot{\delta}$, and $\ddot{\delta}$ as the canard deflection angle, angular velocity, and angular acceleration, respectively. ζ is the damping ratio, ω_n is the system natural frequency, K is a scaling constant, and V_{CMD} is the motor command voltage. This model can be expressed in state space form with state vector $x = \left[\delta, \dot{\delta}\right]^T$ and command input $u(t) = V_{CMD}$ which is a function of time, t.

$$\boldsymbol{x} = \begin{bmatrix}\delta \\ \dot{\delta}\end{bmatrix},\ \dot{\boldsymbol{x}} = \begin{bmatrix}0 & 1 \\ -\omega_n^2 & -2\zeta\omega_n\end{bmatrix}\boldsymbol{x} + \begin{bmatrix}0 \\ \omega_n^2 K\end{bmatrix}u(t) \tag{2}$$

This formulation of the dynamics contains three independent parameters that govern the behavior: ζ, ω_n, and K.

3.2 Nonlinear Dynamic Model

A nonlinear, physics-based dynamic model for the actuator that more accurately captures the inertia, motor, aerodynamics and friction effects is given by the following:

$$I\ddot{\delta} + \mu_1\dot{\delta} + \mu_0 sign\left(\dot{\delta}\right) = \frac{K_T}{R}V_{CMD} + M_{aero}, \tag{3}$$

with δ, $\dot{\delta}$, and $\ddot{\delta}$ as the canard deflection angle, angular velocity, and angular acceleration, respectively. I is the moment of inertia of the dynamic system, μ_1 is a velocity dependent viscous friction term, μ_0 is a constant friction term, K_T is the actuator torque constant, R is the motor resistance, and V_{CMD} is the motor command voltage. The M_{aero} term is the aerodynamic hinge moment on the actuator. The μ_0 term is multiplied by the sign of the angular velocity, so it always opposes motion, but is not dependent on the magnitude of the velocity. Rearranging the terms give the following:

$$\ddot{\delta} = -\frac{\mu_1}{I}\dot{\delta} - \frac{\mu_0}{I} sign(\dot{\delta}) + \frac{K_T}{RI} V_{CMD} + M_{aero}. \quad (4)$$

The model of the dynamics can be expressed in state space form with state vector $\boldsymbol{x} = [\,\delta, \dot{\delta}]^T$ and command input $u(t) = V_{CMD}$, which is a function of time, t. A time delay in the actuator response to a command signal can be modeled using the t_d term to offset the motor command signal as shown:

$$\boldsymbol{x} = \begin{bmatrix}\delta \\ \dot{\delta}\end{bmatrix},\ \dot{\boldsymbol{x}} = \begin{bmatrix}0 & 1 \\ 0 & \frac{-\mu_1}{I}\end{bmatrix}\boldsymbol{x} + \begin{bmatrix}0 \\ \frac{K_T}{RI}\end{bmatrix} u(t - t_d) + \begin{bmatrix}0 \\ \frac{-\mu_0}{I}\end{bmatrix} sign(\boldsymbol{x}) + M_{aero}. \quad (5)$$

For a bench-level test with no hinge moment, the M_{aero} term is zero, resulting in four independent parameters governing this formulation of the dynamic behavior: $\frac{\mu_0}{I}$, $\frac{\mu_1}{I}$, $\frac{K_T}{RI}$, and t_d.

4. Optimal Controller Design

A linear quadratic integrator (LQI) controller is developed to control the actuator position, using the linear state space formulation:

$$\begin{aligned} \dot{\boldsymbol{x}} &= \mathbf{A}\boldsymbol{x} + \mathbf{B}\mathbf{u} \\ \boldsymbol{y} &= \mathbf{C}\boldsymbol{x} + \mathbf{D}\mathbf{u} \end{aligned} \quad (6)$$

Where the state vector $\boldsymbol{x}$, and the **A**, **B**, **C**, **D** matrices are defined from the linear dynamic model:

$$\boldsymbol{x} = \begin{bmatrix}\delta \\ \dot{\delta}\end{bmatrix},\ \mathbf{A} = \begin{bmatrix}0 & 1 \\ -\omega_n^2 & -2\zeta\omega_n\end{bmatrix},\ \mathbf{B} = \begin{bmatrix}0 \\ \omega_n^2 K\end{bmatrix},\ \mathbf{C} = [1 \quad 0],\ \mathbf{D} = 0. \quad (7)$$

The system input, **u**, is the motor voltage, while the system output, y, is the canard deflection angle. The LQI controller uses an augmented state vector given by $\boldsymbol{z} = [\delta \quad \dot{\delta} \quad e_i]^T$, where e_i is the integral of the error between the desired angle, δ_c, and the measured canard deflection, δ. In this application, the integral term

enables the LQI controller to better compensate for external moments such as aerodynamic loads and friction on the canard.

The optimal LQI controller gains, $\boldsymbol{K}$, in the feedback control law, $u = -\boldsymbol{K}\boldsymbol{z}$, are determined by minimizing the quadratic cost function[15,16]:

$$J(u) = \int_0^\infty \{z^T \boldsymbol{Q} z + u^T R u\} dt \tag{8}$$

for a given control effort weighting, R, and a state weighting matrix, $\boldsymbol{Q}$. This cost function is minimized by solving the associated Riccati equation:

$$\mathbf{A}^T\mathbf{S} + \mathbf{S}\mathbf{A} - \mathbf{S}\mathbf{B}R^{-1}\mathbf{B}^T\mathbf{S} + \boldsymbol{Q} = 0, \tag{9}$$

which gives controller gains:

$$\boldsymbol{K} = R^{-1}\mathbf{B}^T\mathbf{S}. \tag{10}$$

The output position of the actuator is measured through the servo potentiometer, but no other state feedback is available; an observer is applied to estimate the full state feedback from the position output using the linear state space dynamic model.[17] The closed-loop eigenvalues for the LQI system are found as

$$\boldsymbol{\lambda_{LQI}} = \boldsymbol{\lambda}(\mathbf{A} - \mathbf{B}\boldsymbol{K}) \tag{11}$$

and the observer gains, $\boldsymbol{L}$, are chosen to place the closed-loop observer eigenvalues 3 to 4 times faster using Ackerman's formula or the Matlab *place* function:

$$3 * Re(\boldsymbol{\lambda_{LQI}}) \leq \boldsymbol{\lambda_{OBS}} \leq 4 * Re(\boldsymbol{\lambda_{LQI}}) \tag{12}$$

$$\boldsymbol{L}^T = place(\mathbf{A}^T, \mathbf{C}^T, \boldsymbol{\lambda_{OBS}}) \tag{13}$$

A block diagram of the architecture of the LQI controller and observer is provided in Fig. 4.

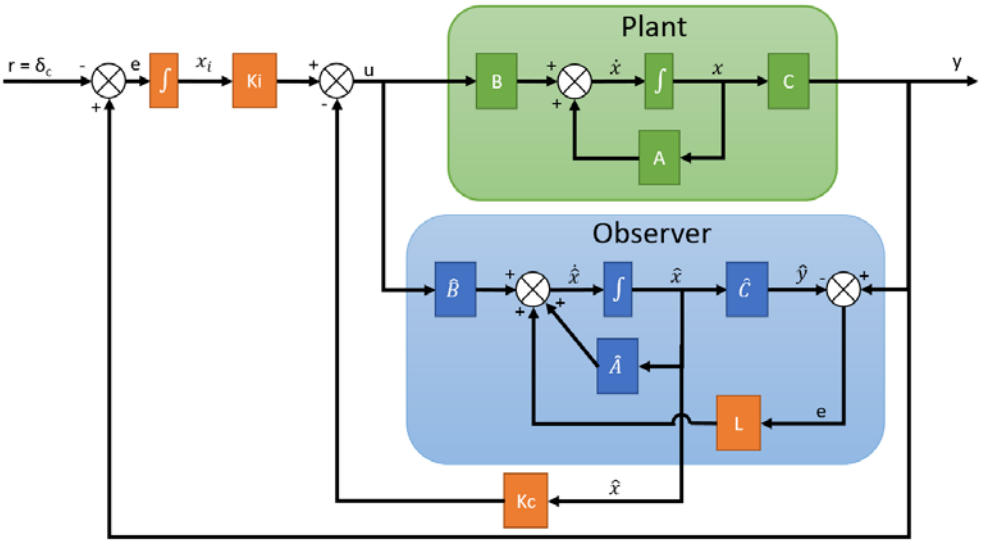

Fig. 4 Block diagram of the LQI controller with observer

5. Dynamic Model Parameter Estimation Algorithm

The parameters for both the linear dynamic model and the physics-based nonlinear dynamic model are estimated from experiments. This multidimensional parameter estimation problem can be approached through several established optimization techniques. This effort uses Particle Swarm Optimization (PSO) to fit the dynamic model simulations to measured open-loop dynamic response data collected through an experiment measuring the actuator response to a series of known motor voltage commands.

PSO is a stochastic optimization technique based on flocking or schooling behavior models and relies on the social sharing of information between individuals in a group in order to optimize an objective function.[18–20] The PSO algorithm consists of a collection of particles, which each have a position and velocity within the parameter space of the problem being studied. Each particle's position corresponds to a candidate solution within the parameter space, and the performance of each candidate solution is evaluated using an objective function. The particles move throughout the parameter space at each timestep of the algorithm, with the velocity of each particle adjusted according to the historical best performance of each individual particle and the best performance of the swarm as a whole.

Define a vector, **x**, comprised of a particular set of parameters within the set of all possible parameter choices contained in the entire design space of the optimization problem. The position of the i^{th} particle in the swarm at time t is given by $\mathbf{x}_t^i$, and the velocity is given by $\mathbf{v}_t^i$. Each particle's performance at the current position in

the design space is determined using an objective function, $\psi(\mathbf{x})$. The historical best position for particle *i* up to time *t* is given by $\mathbf{P}_t^i$, while the global historical best position of any particle in the entire swarm up to time *t* is given by $\mathbf{P}_t^g$. These historical best positions are used to update the velocity of each particle at each timestep according to Eq. 14:

$$\mathbf{v}_{t+1}^i = w\mathbf{v}_t^i + C_1 n_{r_1}\left(\mathbf{P}_t^i - \mathbf{x}_t^i\right) + C_2 n_{r_2}\left(\mathbf{P}_t^g - \mathbf{x}_t^i\right), \tag{14}$$

where the n_{r_1} and n_{r_2} terms are random numbers drawn from a uniform distribution from 0 to 1, and the w, C_1, and C_2 terms are the inertia, self-confidence, and swarm influence weighting factors, respectively, which are used to adjust the behavior of the PSO algorithm.[20] The self-confidence parameter scales the influence of the individual historical best position for each particle, while the swarm influence parameter scales the influence of the global best position. The inertia factor determines how much of the previous velocity is carried over to the next timestep. Following the $t + 1$ velocity calculation, the new position of each particle in the swarm is updated according to the following equation:

$$\mathbf{x}_{t+1}^i = \mathbf{x}_t^i + \mathbf{v}_{t+1}^i. \tag{15}$$

Figure 5 illustrates the velocity calculation and position update for the PSO algorithm.

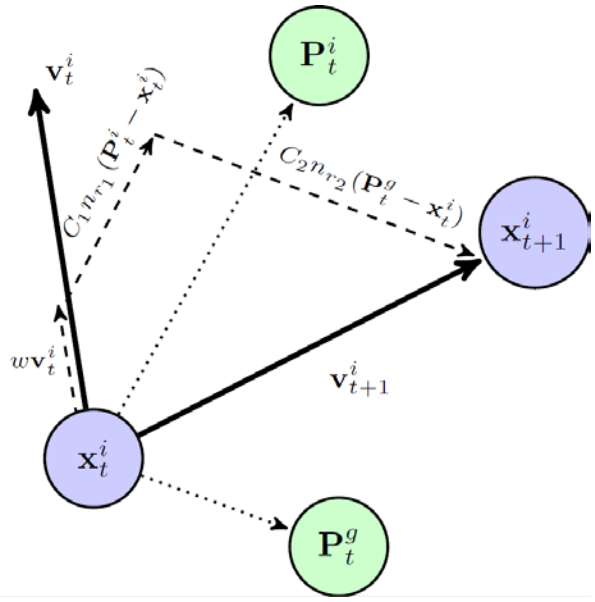

Fig. 5 Illustration of the PSO position update algorithm. The particle position at time t + 1, $\mathbf{x}_{t+1}^i$, is determined by the position at time t, and the velocity at time t + 1, $\mathbf{v}_{t+1}^i$. The $\mathbf{v}_{t+1}^i$ term comprises vector components along the previous velocity, $\mathbf{v}_t^i$, as well in the directions of the historical best and global best positions.

6. Experimental Apparatus

A benchtop experimental apparatus is used to study the actuator dynamics, develop the dynamic models, and verify the controller. EFLRDS76T servos are modified by removing the stock electronics and exposing the motor and potentiometer wires for direct access. A Texas Instruments (TI) 320F28335 DSP is used to generate a 10-kHz pulse-width modulated signal, which is sent through a TI DRV8835 dual H-bridge motor driver to supply the servo motor with a controllable voltage ranging from +8 to –8 V. The servo potentiometer is sampled using a 12-bit analog-to-digital converter on the DSP. The DSP is configured to record motor voltage command and servo potentiometer measurements at a rate of 1 kHz and save the data for postprocessing and analysis. Figure 6 shows the DSP and support electronics, as well as modified servos installed in the CAS module, with one servo driving a canard blade through a linkage. This setup does not include the aerodynamic loading described in Section 3.

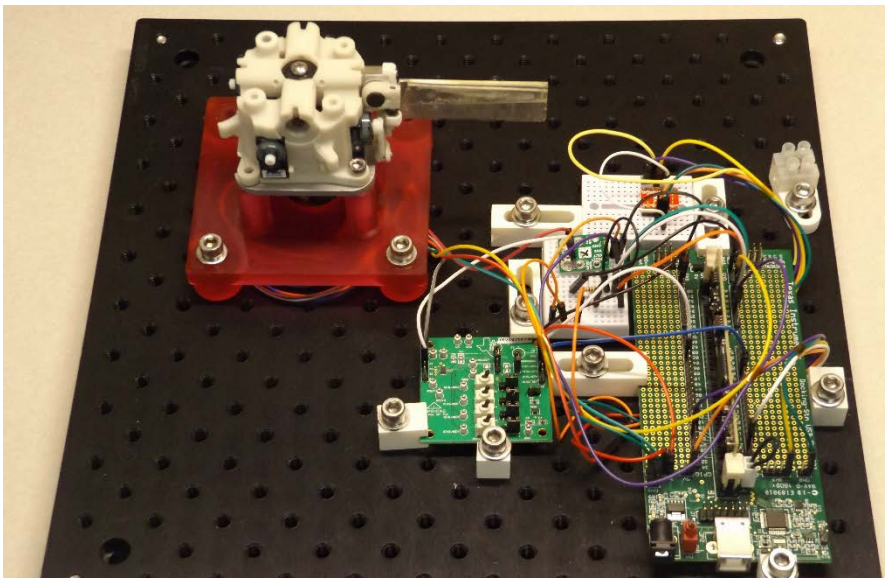

Fig. 6 Benchtop experiment apparatus showing the DSP controlling a modified servo to drive a canard, along with the supporting electronics

7. Open-Loop Dynamic Response

To collect open-loop dynamic response data for the actuator, the DSP and motor driver were used to apply short voltage pulses of varying amplitude and duration to the actuator servo motor while the DSP recorded the actuator position through the servo potentiometer. The input signals and subsequent actuator responses are shown in Fig. 7, in which each plot presents the measured response of six individual trials, along with the average response.

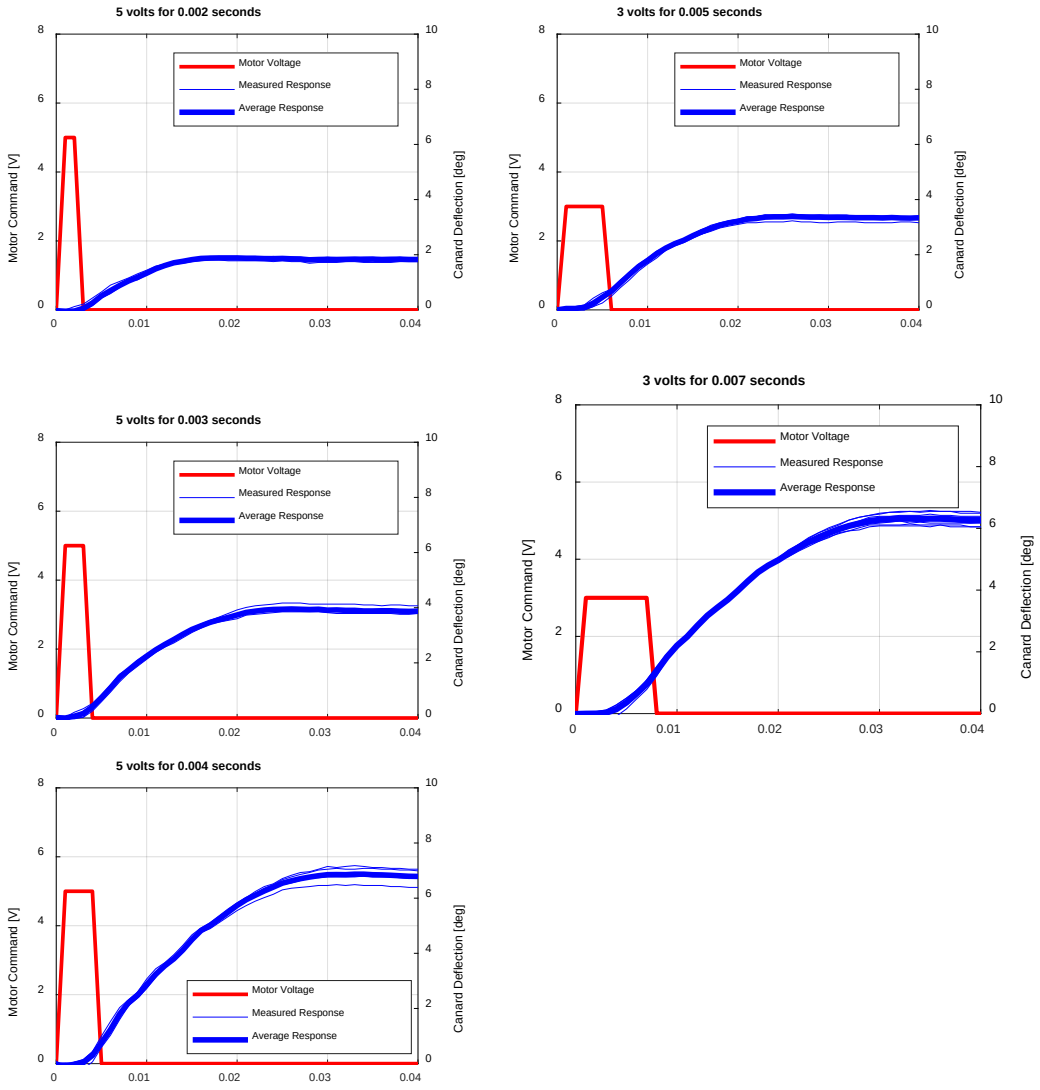

Fig. 7 Open-loop response of the actuator showing the canard blade deflection change resulting from a given voltage pulse applied to the servo

8. Dynamic Model Parameter Estimation Using PSO

The measured open-loop dynamic responses are used to estimate the parameters of the linear and nonlinear dynamic models. The PSO algorithm is applied to identify parameter values for each dynamic model that result in model behavior closely matching the measured open-loop response.

Two separate estimation analyses are performed; for the linear dynamic model the estimation seeks parameters ζ, ω_n, and K, while a separate estimation effort seeks parameters $\frac{\mu_0}{I}$, $\frac{\mu_1}{I}$, $\frac{K_T}{RI}$, and t_d to populate the nonlinear dynamic model. The estimation for the linear model has particles with position vectors $\mathbf{x} \in \mathbb{R}^3$ with the

valid parameter values in each dimension bounded by the values in Table 1 to scope the search space of the optimization algorithm. Similarly, the estimation for the nonlinear dynamic model has particles with position vectors $\mathbf{x} \in \mathbb{R}^4$, likewise limited to the ranges given in Table 2.

Table 1 Parameter range for the linear dynamic model

Linear model parameter	Range
ζ	[0.1, 0.9]
ω_n	[1, 200]
K	[1, 100]

Table 2 Parameter range for the nonlinear dynamic model

Nonlinear model parameter	Range
$\frac{\mu_0}{I}$	[1e3, 1e6]
$\frac{\mu_1}{I}$	[0, 100]
$\frac{K_T}{RI}$	[1e3, 1e6]
t_d	[0, 0.003]

The PSO algorithm requires an objective function to evaluate the relative performance of each particle at each timestep. The objective function for this research is chosen to be the root-sum-square of the error between the experimental response and the simulated response of the dynamic model:

$$\psi(\mathbf{x}) = \sqrt{\sum_{i=1}^{n} \sum_{t=0}^{t_f} \left(\delta_{meas}^{i}(t) - \delta_{model}^{i}(t) \right)^2}, \qquad (16)$$

where $\delta_{meas}^{i}(t)$ is the average measured canard position at timestep *t* from the i^{th} open-loop experiment of n experiments, and $\delta_{model}^{i}(t)$ is the simulated canard position at time *t*, obtained by numerical integration of the dynamic model using the motor inputs from the i^{th} open-loop experiment. In this way, the dynamic models are simulated against all five open-loop experimental responses simultaneously, to identify model parameters that reflect the actuator behavior across a range of inputs.

The PSO adjustment coefficients were chosen based on standard best practices,[20] and the swarm size was chosen to be 100 and 500 for the three and four parameter estimation problems, respectively, as shown in Table 3.

Table 3 PSO coefficients for the parameter estimation analysis

PSO parameter	Linear model estimation	Nonlinear model estimation
Swarm size	100	500
w	1.0	1.0
C_1	2.0	1.5
C_2	1.0	1.5

The best-performing parameter set identified by the optimization for the linear dynamic model is given in Table 4. The response of the linear dynamic model with the parameters in Table 4 is plotted in Fig. 8 alongside the average measured actuator response for all five open-loop test cases. This linear dynamic model provides a reasonable approximation of the transient portion of the actuator response to motor inputs across the test cases but is unable to capture the transition to steady state.

Table 4 Best-performing parameter set for linear dynamic model

Linear model parameter fit: $\boldsymbol{\psi(\mathbf{x}) = 12.698}$	
Parameter	**Value**
ζ	0.54974
ω_n	39.525
K	14.487

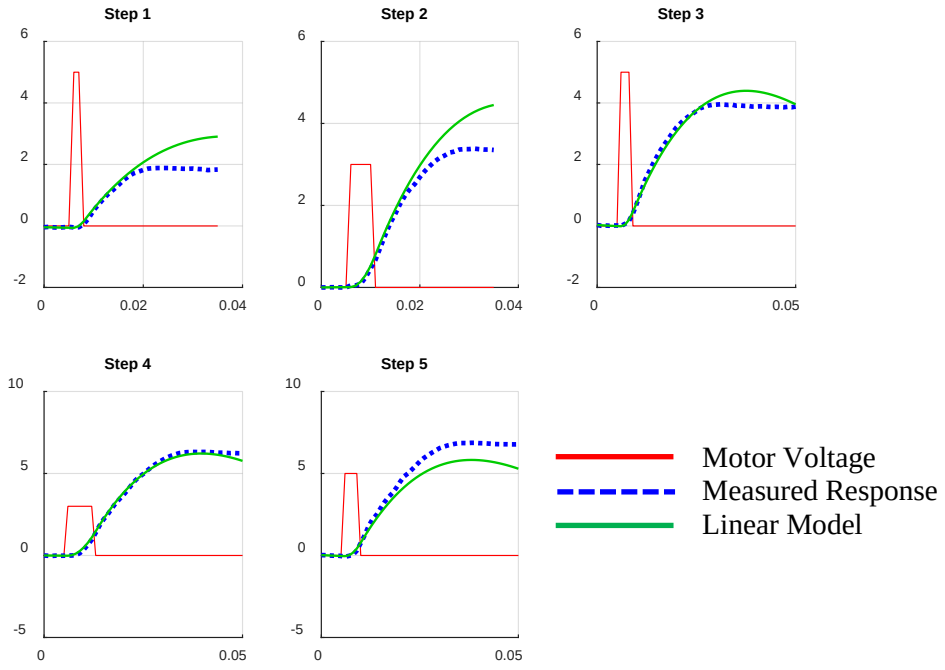

Fig. 8 Best-performing linear model response to the applied motor voltage pulse, compared to measured open-loop response of the actuator

The best-performing parameter set identified by the optimization for the nonlinear dynamic model is given in Table 5, with the response plotted in Fig. 9 alongside the average measured actuator response for all five open-loop test cases. Compared to the linear model, this nonlinear model is able to better capture the dynamics (e.g., inertia, motor, friction effects) and provides a much closer match to the measured response to motor inputs.

Table 5 Best-performing parameter set for the nonlinear dynamic model

Nonlinear model parameter fit $\boldsymbol{\psi(\mathbf{x}) = 4.0295}$	
Parameter	**Value**
$\frac{\mu_0}{I}$	20877
$\frac{\mu_1}{I}$	–8.5528
$\frac{K_T}{RI}$	25922
t_d	0.0007471

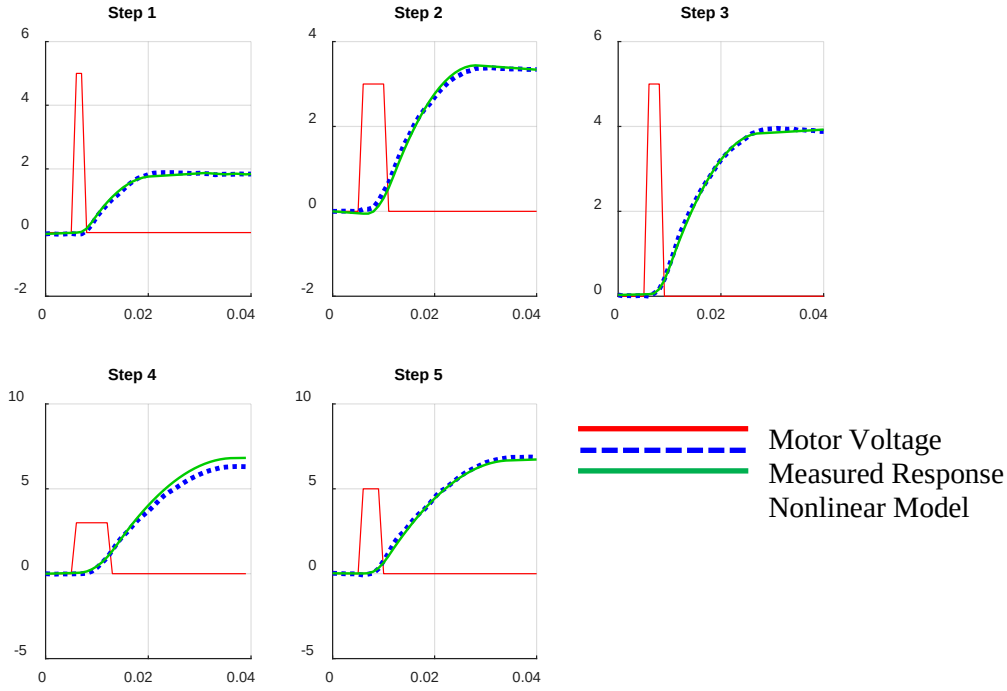

Fig. 9 Best-performing nonlinear model response to the applied motor voltage pulse, compared to measured open-loop response of the actuator

9. Modeled Closed-Loop Actuator Response

The dynamic performance objectives for the CAS are a rise time, T_r, of 15 ms and a settling time, T_s, of 25 ms for a 10° canard deflection step. To achieve these objectives, the LQI controller design algorithm is iterated while incrementally decreasing the control input weighting term, R. The closed-loop response is simulated using the nonlinear dynamic model for each LQI controller iteration, and T_r and T_s of the modeled response are compared to the objectives. The process is iterated while gradually increasing control effort until the performance objectives are met.[14]

The controller design algorithm is populated using the linear dynamic model from Eq. 1 and the parameters identified in Table 4. The *R* and $\boldsymbol{Q}$ weights are initialized as follows:

$$R = 1,\ \boldsymbol{Q} = \begin{bmatrix} 1 & 0 & 0 \\ 0 & 0 & 0 \\ 0 & 0 & 1e6 \end{bmatrix}, \tag{17}$$

with the $\boldsymbol{Q}$ matrix terms chosen to place emphasis on minimizing the integration error term. The optimal LQI controller gain vector that satisfies the T_r and T_s objectives is found to be

$$\boldsymbol{K} = [9.5396 \quad 0.025182 \quad -1429.4] , \tag{18}$$

with observer gains of

$$\boldsymbol{L} = [\ 1.4555 \quad 508.52\ ]^T . \tag{19}$$

The LQI controller and observer are implemented on both the linear and nonlinear actuator models, and the closed-loop dynamics are simulated for step input commands of 5° and 10°. The closed-loop responses of both dynamic models to the step input commands are shown in Fig. 10.

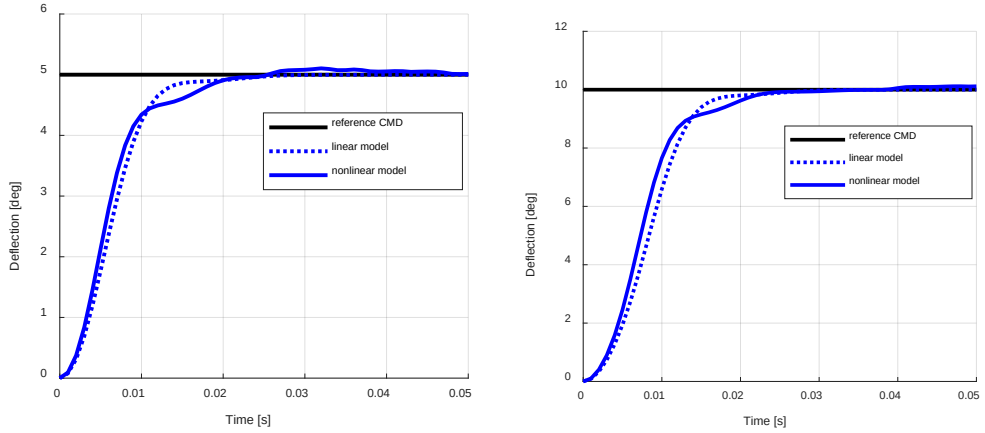

Fig. 10 Closed-loop response of the LQI controller applied to both the linear and nonlinear dynamic models

The rise time and settling time for the modeled responses for each input command are given in Table 6. In each case, the modeled response satisfies the actuator performance objective.

Table 6 Rise time and settling time for linear and nonlinear models with LQI controller

Controller performance	$\boldsymbol{T_r}$	$\boldsymbol{T_s}$
Objective (max)	0.015	0.025
Linear model response (5°)	0.008616	0.019031
Linear model response (10°)	0.010242	0.019791
Nonlinear model response (5°)	0.010234	0.020051
Nonlinear model response (10°)	0.010329	0.021891

10. Measured Closed-Loop Actuator Response

The LQI controller was implemented on the DSP, and an experiment was performed to measure the closed-loop dynamic response of the actuator. Step input commands of 5° and 10° were applied, and the actuator response was measured through the servo potentiometer and recorded using the DSP.

Figure 11 plots 10 measured responses to an input command of 5° and 10 measured responses to a 10° input command, along with the average measured response for each input.

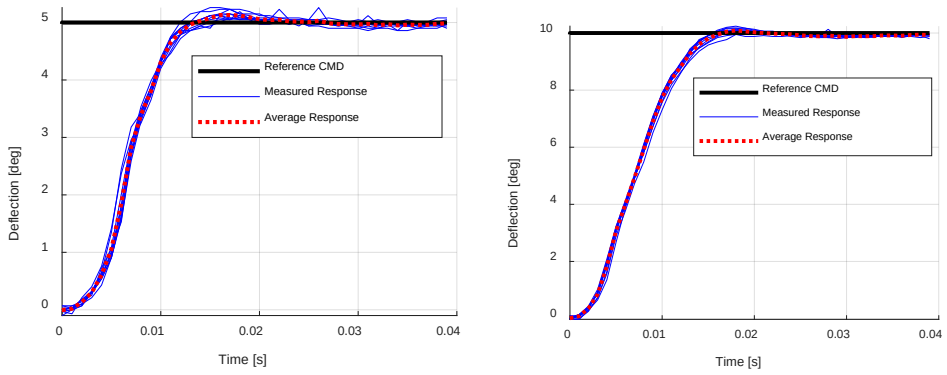

Fig. 11 Measured response to step input commands for the closed-loop actuator with the LQI controller implemented

The rise time and settling time for the measured responses for each input command are given in Table 7. In each case, the measured response satisfies the objective actuator performance goals.

Table 7 Measured rise time and settling time of the closed-loop actuator with the LQI controller implemented

Controller performance	T_r	T_s
Objective (max)	0.015	0.025
Measured response (5°)	0.0069058	0.024679
Measured response (10°)	0.0092483	0.020955

11. Conclusion

This report presented canard control technology research seeking a low-cost, fast-responding, high-g tolerant actuator built around COTS servos that meets flight performance requirements. Linear and nonlinear actuator dynamic models were presented, along with the controller architecture. The nonlinear dynamic model captures more effects such as friction to more closely predict the actuator behavior, and can be used to improve the fidelity of actuator models in both stand-alone analysis and munition flight simulation analysis. The linear dynamic model was used to design an LQI controller and observer to meet the CAS actuator performance objectives. An open-loop experiment was performed to populate the dynamic model coefficients. This controller was implemented in hardware, and an experiment was performed to demonstrate the closed-loop response of the actuator satisfies the design objectives.

12. References

1. Carlucci DE, Frydman AM, Cordes JA. Mathematical description of projectile shot exit dynamics (set forward). Journal of Applied Mechanics. 2013;80(3):031501:1–9.

2. Bender JM. Structural analysis of the Excalibur canard actuation system and the guidance and navigation unit. Adelphi (MD): Army Research Laboratory (US); 2008. Report No.: ARL-TR-4412.

3. General Dynamics Ordnance and Tactical Systems. Missile Components. Control Actuator Systems (CAS). St Petersburg (FL): General Dynamics; c1995–2018 [accessed 2018 Aug 24]. https://www.gd-ots.com/missiles-and-rockets/missile-components/control_actuator_systems/.

4. Fresconi FE, Harkins T, Experimental flight characterization of asymmetric and maneuvering projectiles from elevated gun firings. Journal of Spacecraft and Rockets. 2012;49(6):1120–1130.

5. Fresconi FE. Guidance and control of a projectile with reduced sensor and actuator requirements. Journal of Guidance, Control, and Dynamics. 2011;34(6):1757–1766.

6. Fresconi FE, Brown G, Celmins I, DeSpirito J, Ilg M, Maley J, Magnotti P, Scanlan A, Stout C, Vazquez E. Very affordable precision projectile technology development and flight demonstrations. Aberdeen Proving Ground (MD): Army Research Laboratory (US); 2011. Report No.: ARL-TR-5460.

7. Fairfax L, Fresconi F, Maley J, inventors; US Secretary of Army, assignee. Method and apparatus for GPS-denied navigation of spin-stabilized projectiles. United States patent US 9,702,674. 2017 July 11.

8. McMichael J, Lovas A, Plostins P, Sahu J, Brown G, Glezer A. Microadaptive flow control applied to a spinning projectile, Aberdeen Proving Ground (MD): Army Research Laboratory (US); 2005. Report No.: ARL-TR-3589.

9. Gnemmi P, Rey C. Plasma actuation for the control of a supersonic projectile. Journal of Spacecraft and Rockets. 2009;46(5):989–998.

10. Kim D, Strickland L, Gross M, Rogers J, Costello M, Fresconi F, Celmins I. Actuator design and flight testing of an active microspoiler-equipped projectile. ASME. J Dyn Sys, Meas, Control. 2017;139(11):111002-111002-15. doi:10.1115/1.4036808.

11. Celmins I. Design and evaluation of an electromechanical actuator for projectile guidance. Aberdeen Proving Ground (MD): Army Research Laboratory (US); 2007. Report No.: ARL-MR-0672.

12. Weinacht P. Coupled CFD/GN&C modeling for a smart material canard actuator. Aberdeen Proving Ground (MD): Army Research Laboratory (US); 2007. Report No.: ARL-TR-4265.

13. Fresconi FE, Celmins I, Silton S, Costello M. High maneuverability projectile flight using low cost components. Aerosp Sci Technol. 2015;41:175–188.

14. Burchett B. Matlab tools for automated system identification and control design of single-input single-output (SISO) motor loops. Aberdeen Proving Ground (MD): Army Research Laboratory (US); 2017. Report No.: ARL-CR-0817.

15. Young PC, Willems JC. An approach to the linear multivariable servomechanism problem. International Journal of Control. 1972;15(5): 961–979.

16. Katayama T, Hirono T. Design of an optimal servomechanism with preview action and its dual problem. International Journal of Control. 2007;45(2):407–420.

17. Kautsky J, Nichols NK, Van Dooren P. Robust pole assignment in linear state feedback. International Journal of Control. 1985;41:1129–1155.

18. Kennedy J, Eberhart R. Particle swarm optimization. Proceedings of ICNN'95 - International Conference on Neural Networks; 1995 Nov 27–Dec 1; Perth, Australia. IEEE. 1995;4:1942–1948.

19. Perez RE, Behdinan K. Particle swarm optimization in structural design. In: Chan FTS, Tiwari, MK, editors. Swarm intelligence, focus on ant and particle swarm optimization. InTechOpen. 2007 Dec 1. Chapter 22. doi: 10.5772/5114.

20. Hassan R, Cohanim BE, de Weck OL, Venter G. A comparison of particle swarm optimization and the genetic algorithm. Proceedings of the 46th AIAA/ASME/ASCE/AHS/ASC Structures, Structural Dynamics, and Materials Conference; 2005 Apr 18–21; Austin, TX. Paper No.: AIAA-2005-1897.

List of Symbols, Abbreviations, and Acronyms

CAS	control actuation system
COTS	commercial off-the-self
DSP	digital signal processor
HMA	high-maneuverability airframe
LQI	linear quadratic integrator
PSO	Particle Swarm Optimization
TI	Texas Instruments

1 (PDF) DEFENSE TECHNICAL INFORMATION CTR DTIC OCA

2 (PDF) DIR ARL IMAL HRA RECORDS MGMT RDRL DCL TECH LIB

1 (PDF) GOVT PRINTG OFC A MALHOTRA

1 (PDF) ARL RDRL WML E J BRYSON